

An Integrated Framework to Quantitatively Link Mouse-Specific Hemodynamics to Aneurysm Formation in Angiotensin II-infused ApoE $-/-$ mice

BRAM TRACHET,¹ MARJOLIJN RENARD,² GIANLUCA DE SANTIS,¹ STEVEN STAELENS,^{3,4} JULIE DE BACKER,² LUCA ANTIGA,^{5,6} BART LOEYS,^{2,7} and PATRICK SEGERS¹

¹IBiTech-bioMMeda, Ghent University, De Pintelaan 185, Block B, 9000 Ghent, Belgium; ²Centre for Medical Genetics, Ghent University, Ghent, Belgium; ³IBiTech-Medisip, Ghent University—IBBT, Ghent, Belgium; ⁴Molecular Imaging Center, Antwerp University, Antwerp, Belgium; ⁵Orobix Srl, Bergamo, Italy; ⁶Department of Bioengineering, Mario Negri Institute, Bergamo, Italy; and ⁷Centre of Medical Genetics, Antwerp University Hospital, Antwerp, Belgium

(Received 1 April 2011; accepted 14 May 2011; published online 26 May 2011)

Associate Editor Joan Greve oversaw the review of this article.

Abstract—Locally disturbed flow has been suggested to play a (modulating) role in abdominal aortic aneurysm (AAA) formation, but no longitudinal studies have been performed yet due to (a.o.) a lack of human data prior to AAA formation. In this study we made use of recent advances in small animal imaging technology in order to set up entirely mouse-specific computational fluid dynamics (CFD) simulations of the abdominal aorta in an established ApoE $-/-$ mouse model of AAA formation, combining (i) *in vivo* contrast-enhanced micro-CT scans (geometrical model) and (ii) *in vivo* high-frequency ultrasound scans (boundary conditions). Resulting areas of disturbed flow at baseline were compared to areas of AAA at end-stage. Qualitative results showed that AAA dimension is maximal in areas that are situated proximal to those areas that experience most disturbed flow in three out of four S developing an AAA. Although further quantitative analysis did not reveal any obvious relationship between areas that experience most disturbed flow and the end-stage AAA dimensions, we cannot exclude that hemodynamics play a role in the initial phases of AAA formation. Due to its mouse-specific and *in vivo* nature, the presented methodology can be used in future research to link detailed and animal-specific (baseline) hemodynamics to (end-stage) arterial disease in longitudinal studies in mice.

Keywords—Mouse-specific hemodynamics, Computational fluid dynamics, Abdominal aortic aneurysm, ApoE $-/-$ mouse model, Contrast-enhanced micro-CT, High-frequency ultrasound.

INTRODUCTION

The pathogenesis and “natural history” of aortic aneurysm formation are still not fully understood. Despite the fact that known risk factors such as old age, male gender, smoking, hypertension or genetic predisposition are of a systemic nature, aneurysms tend to occur at a limited number of aortic sites. A typical example is the abdominal aortic aneurysm (AAA), that (in humans) most often develops in the infrarenal region of the abdominal aorta. Several theories have been proposed over the years to explain the specific local nature of this phenomenon.^{1,30,31} The human infrarenal abdominal aorta is believed to be a region of low mean and oscillatory wall shear stresses,²⁹ hemodynamic conditions that have been shown to be related to the onset of atherosclerosis.^{23,26} Furthermore there is anecdotal evidence for a relationship between disturbed flow and AAA formation in patients with spinal cord injury^{20,41} and patients with one amputated leg.⁴⁰ Therefore, one theory on the location of AAA formation hypothesizes that biomechanical factors related to the forces induced by the blood flow on the endothelium (low shear stress levels and/or oscillatory blood flow patterns) interplay with vascular biology. However, this theory has never been tested in a longitudinal study comparing hemodynamic conditions pre- and post-AAA.

To assess the aforementioned biomechanical factors related to the blood flow, one requires detailed information on the 3-dimensional flow field with a high resolution both in time and in space. It is feasible to measure flows in the aorta using either ultrasound or MRI, but neither of these techniques provides a

Address correspondence to Bram Trachet, IBiTech-bioMMeda, Ghent University, De Pintelaan 185, Block B, 9000 Ghent, Belgium. Electronic mail: bram.trachet@ugent.be

resolution (in time nor space) that would allow to study the flow field in sufficient detail to assess the shear forces directly. To overcome this problem, computational fluid dynamics (CFD) can be used to resolve the flow field in the abdominal aorta. For this purpose one typically needs (i) an accurate 3D geometrical model and computational mesh of the abdominal aorta and major side branches; (ii) precise information on the inflow and outflows (boundary conditions) in each branch. This information should be patient-specific and preferentially measured *in vivo*. Patient-specific CFD results at baseline, if available, can then be compared to AAA location in the end-stage geometry of the same patient.

Unfortunately, it is virtually impossible to monitor the genesis and progression of an aneurysm in humans throughout their life. The main reason for this is the fact that most AAA is asymptomatic and as such there are no baseline data in almost all clinical cases. Moreover disease progression often takes several decades, another complicating factor in the study of the natural history.¹⁹ Given these limitations in human research animal models in general, and mouse models in particular, are therefore a suitable alternative to unravel the potential role of these biomechanical factors in aneurysm development. The most well studied mouse model for AAA is probably the ApoE knockout mouse model which, when continuously infused with Angiotensin II with an implanted osmotic pump, leads to development of an abdominal aneurysm.¹⁰ This mouse model has been used in several studies to assess, e.g., the different stadia of aneurysm formation *ex vivo*³² or the morphometric evolution of the aortic diameter over time *in vivo*.⁵ A remarkable observation is that the AAA in this mouse model develops in the suprarenal region in contrast to the infrarenal region in humans.⁹ The debate as to why this is the case is still ongoing. It has been shown that the suprarenal region has a higher degree of curvature (bending to the left) that appears to correlate with the direction of vessel motion over the cardiac cycle and direction of average AAA expansion (both of which also appear leftward).¹⁷ Another study showed that ApoE $-/-$ mice, as opposed to humans, do not experience reversed flow in the infrarenal abdominal aorta.² The latter observation was based on MRI measurements of aortic volumetric blood flow rate, but did not include CFD simulations to study the local hemodynamics in detail. Until recently, the limiting factor for such studies was the lack of temporal and spatial resolution in the available imaging modalities. In literature, most CFD simulations working with murine data base their arterial geometry on a vascular cast (excluding longitudinal studies) and the applied boundary conditions are often generic (e.g., applying a fixed volumetric flow rate).^{14,22,36,37} Recent advances in

imaging technology have, however, allowed to circumvent these limitations.³⁸

In this study, we developed an experimental-computational framework combining information from both contrast-enhanced micro-CT (arterial geometry) and high-frequency ultrasound (boundary conditions) to set up mouse-specific CFD simulations allowing to study the hemodynamic situation in the abdominal aorta in a detailed way. For each mouse included in the study a representative set of volumetric flow rates (compatible with each other throughout the cardiac cycle) going to all abdominal branches is presented. Moreover, using a previously described mouse model of AAA formation¹¹ we compared hemodynamics in the abdominal aorta at baseline—i.e., before the aneurysm is initiated—to the location of the aneurysm in the end-stage geometry.

MATERIALS AND METHODS

Mice

Ten in-house bred male ApoE $-/-$ mice on a C57Bl6 background (age 12 ± 3 weeks; other data: see Table 1) were included in this study. They were housed in separate cages and water and regular mouse diet were available *ad libitum*. As previously described¹¹ these mice were implanted an osmotic pump (model Alzet 2004; Durect Corp, Cupertino, CA), filled with Angiotensin II (Bachem, Bubendorf, Switzerland). To avoid interference with the micro-CT images, the metal flow divider inside the pump was replaced by a PEEK alternative (Durect Corp, Cupertino, CA). Each pump released its content over a period of 28 days, at an infusion rate of $1000 \text{ ng kg}^{-1} \text{ min}^{-1}$. Pumps were implanted subcutaneously on the right flank via an incision in the scapular region. Mice were observed daily after the implantation of pumps. Ultrasound and micro-CT scans (see below for details) were obtained at baseline (before pump implantation) and at end-stage (31 days after pump implantation). After the last scan, the animals were euthanized and the abdominal aorta was dissected. Images of the dissected AAA region were taken using an Olympus microscope equipped with a 5 MPixel camera. All experiments were in accordance with EC guidelines for animal research and were approved by the animal ethics committee of the Ghent University.

In vivo Imaging

Micro-CT

At each scanning timepoint, animals were anesthetized with 1.5% isoflurane and, once anesthetized,

TABLE 1. Baseline data for all studied mice.

Mouse ID	BW (g)	HR (bpm)	Average flow [mL/s (%)]						Diameter (mm)					
			PAA	CA	MA	RRA	LRA	DAA	PAA	CA	MA	RRA	LRA	DAA
AA1 ^a	29.0	424	1.65	0.11 (7)	0.25 (15)	0.54 (33)	0.41 (25)	0.34 (21)	1.48	0.41	0.66	0.71	0.55	0.87
AA2 ^a	29.9	423	1.05	0.11 (10)	0.22 (22)	0.05 (5)	0.19 (19)	0.47 (45)	1.27	0.52	0.76	0.54	0.43	0.77
AA4 ^a	23.1	512	1.18	0.12 (11)	0.40 (34)	0.16 (13)	0.21 (18)	0.28 (24)	1.18	0.37	0.59	0.42	0.46	0.76
AA5	24.8	458	1.21	0.15 (12)	0.30 (25)	0.33 (28)	0.20 (16)	0.23 (19)	1.09	0.40	0.51	0.54	0.38	0.57
AA6	23.9	514	1.62	0.18 (11)	0.37 (23)	0.47 (29)	0.21 (13)	0.32 (20)	1.18	0.50	0.71	0.56	0.41	0.80
AA7	22.0	392	1.14	0.17 (15)	0.40 (35)	0.15 (13)	0.13 (11)	0.30 (26)	1.21	0.43	0.67	0.51	0.41	0.77
AA8	23.6	403	2.34	0.18 (8)	0.99 (43)	0.49 (21)	0.25 (11)	0.42 (18)	1.34	0.43	0.69	0.65	0.50	0.67
AA9	21.4	438	1.60	0.15 (9)	0.35 (22)	0.35 (22)	0.22 (14)	0.53 (33)	1.28	0.40	0.60	0.53	0.49	0.70
AA10 ^a	21.5	435	1.46	0.16 (11)	0.61 (42)	0.16 (11)	0.13 (9)	0.40 (27)	1.16	0.45	0.66	0.37	0.28	0.68
Mean	24.4	444	1.47	0.15 (10)	0.43 (29)	0.30 (20)	0.22 (15)	0.36 (25)	1.24	0.43	0.65	0.54	0.43	0.73
Stdev	3.1	43	0.40	0.03 (2)	0.24 (10)	0.18 (9)	0.08 (5)	0.10 (9)	0.12	0.05	0.07	0.10	0.08	0.09

Indicated volumetric flow rate data going to each branch are the redistributed flows as they were imposed in the CFD simulations. All volumetric flow rate values are averaged over a cardiac cycle. The fraction of the volumetric flow rate going to each side branch is indicated between brackets.

HR heart rate, BW body weight, Stdev standard deviation, PAA proximal abdominal aorta, CA celiac artery, MA mesenteric artery, RRA right renal artery, LRA left renal artery, DAA distal abdominal aorta.

^aMouse developed an AAA.

injected intravenously in the lateral tail vein with 100 microliter/25 g of Aurovist (Nanoprobes, Yaphank, NY). As the contrast is maximal immediately after injection, the animals were subsequently scanned in supine position in a GE FLEX Triumph CT scanner (Gamma Medica-Ideas, Northridge, CA, USA). The acquisition parameters were the following: 50 μ m focal spot, 2 \times 2 detector binning, 1024 projections over 360°, 3.5 times magnification, and 70 kVp tube voltage. Using a blank air scan, the ideal tube current was determined by increasing the current until the detector response saturated. This ideal tube current was determined at 180 μ A for a 70 kVp tube voltage. The gantry rotated continuously, providing faster acquisition compared to step-and-shoot mode. This results in a 33.81 mm transverse field of view, a theoretical spatial resolution of 46 μ m and a scanning time of 4.26 min. The projections were reconstructed with proprietary software (Cobra EXXIM, EXXIM Computing corp., Livermore, USA) using a Feldkamp-type algorithm with Parker's weighting function in a 512 \times 512 \times 512 matrix with a 75 μ m voxel size.

Ultrasound

After the micro-CT scan, anesthesia was maintained and mice immediately underwent an ultrasound scan. Ultrasound data were obtained with a high-frequency ultrasound apparatus (Vevo 2100, Visualsonics, Toronto, Canada) equipped with a linear array probe (MS 550D, frequency 22–55 MHz) and mouse handling table. All measurements were performed by a unique operator. The animal was secured on the table in supine position and ECG and respiratory rate were

monitored via four electrodes connected to the paws of the animal while body temperature was monitored via a rectal probe. The ultrasound protocol was restricted to 1 h per mouse. First, B-mode imaging of the abdominal aorta and side branches was performed followed by pulsed Doppler to assess flow velocities at proximal (inflow) and distal (outflow) abdominal aorta, with angle correction upon measurement. To enable correlation of flow velocity measurements with diameters obtained in micro-CT, the distance from (a) the location of proximal aortic flow velocity measurement to the bifurcation of the celiac artery and (b) the location of distal aortic flow velocity measurement to the bifurcation of the mesenteric artery was measured along the aorta. Color Doppler imaging was used to locate celiac, mesenteric and left and right renal arteries, and pulsed Doppler was used to assess flow velocities in these side branches of the abdominal aorta (with angle correction upon measurement). Each flow velocity measurement in the side branches was performed at two locations: the first one immediately after branching, and the second more distally in the branched artery. For each pulsed Doppler measurement the distance from the measurement location to its originating bifurcation was measured along the branch.

Processing Imaging Data

Micro-CT

Reconstructed images were converted into DICOM standard format, and imported into the 3D segmentation software package Mimics (Materialise, Leuven, Belgium). The abdominal aorta and its four major

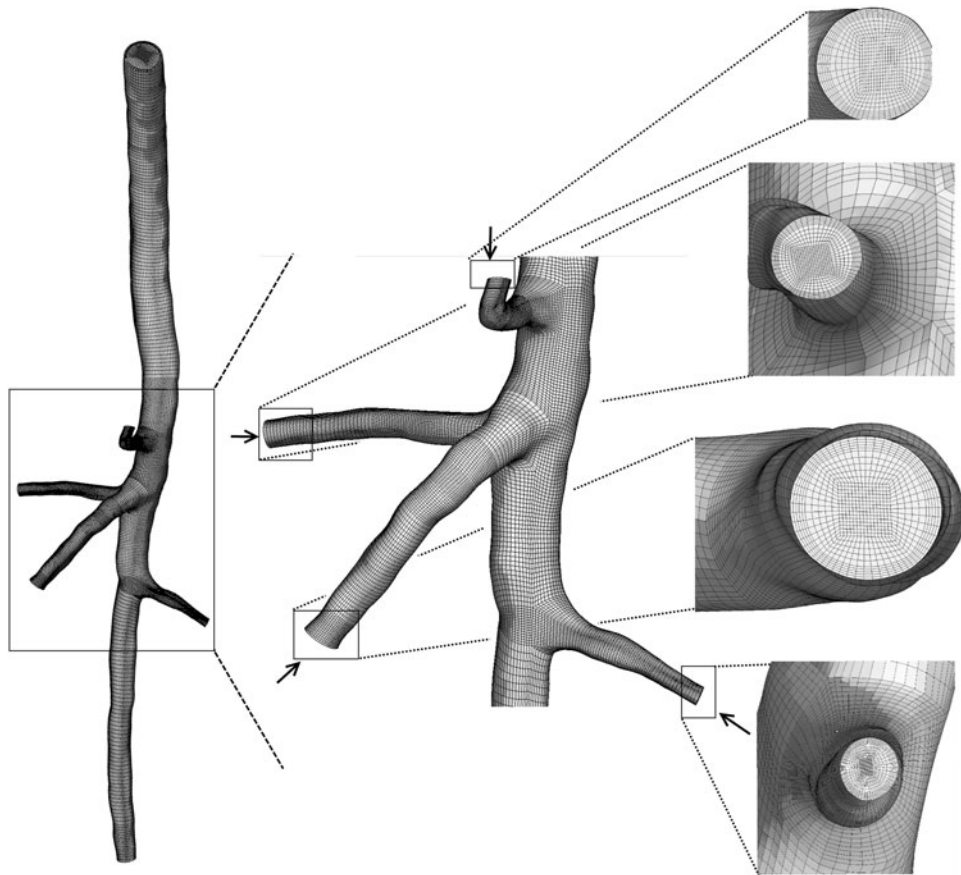


FIGURE 1. A conformal hexahedral mesh is generated to be used as a geometrical model in the CFD simulations.

branches (celiac, mesenteric, left, and right renal arteries) were semi-automatically segmented using the built-in segmentation tools, with as final result a 3D reconstruction of the abdominal aorta. All superfluous parts at inlet and outlets were removed and the surface was smoothed to remove occasional artifacts such as bulges and dents. The luminal surface, represented as triangular grid, was processed in pyFormex³⁹ to generate a structured and conformal fully hexahedral mesh inside the aortic flow domain, allowing higher accuracy than unstructured meshes, thanks to a lower numerical diffusion error in the CFD calculations.¹³ Briefly, the mesh was generated using a multi-block approach, in which hexahedral cells were aligned longitudinally along the vessel centerlines and combined together in a conformal fashion at locations of branching, both for bi- and trifurcations. We refer to Fig. 1 for an example of the mesh used for the flow computations.

Ultrasound

Doppler flow velocity spectra were automatically traced using the built-in analysis tools of the Visual-

sonics software and subsequently exported for further analysis in dedicated software tools (Matlab, Natick, MA). These time-series, containing multiple beats, were first converted into an ensemble averaged flow velocity waveform. To do so, the R-peak of the ECG-signal was used to mark the start and ending of a cardiac cycle. A minimum of three cycles was selected, and one representative average flow velocity waveform was obtained.

Since flow velocity is not constant throughout an arterial segment (due to the tapering) and as the boundary conditions in the CFD model were not always applied at the exact same location where flow velocity was measured, a conversion to volumetric flow rate was mandatory. For this purpose the diameter at the location of the flow velocity measurement was measured in the reconstructed 3D model of the artery (based on the micro-CT scans). To determine the location of the flow velocity measurement on the 3D model, the distance along the aorta was used. Volumetric flow rate was then obtained by multiplying flow velocity with the local cross-sectional area and dividing by 2, assuming that velocity profiles are parabolic and that pulsed wave Doppler measures the peak of the

parabolic flow profile. For the four side branches, in general the average between the proximal and distal measurement was used when both were available.

These calculations lead to one volumetric flow rate waveform (proximal aorta) used as input, and five volumetric flow rate waveforms that could potentially be used as output boundary conditions. Since the flow velocity measurements in different branches were not obtained simultaneously, small differences in heart rate occurred for all volumetric flow rate waveforms. Therefore, the average heart cycle duration over all waveforms was calculated and all waveforms were resampled and scaled in time to match this heart cycle duration. Furthermore, as the CFD simulations are performed assuming rigid walls,

it is essential that at any timepoint, the input equals the sum of the output volumetric flow rates (dotted lines in Fig. 2c) to balance the conservation of mass. To ensure that this was effectively the case, the difference between the measured volumetric outflow rate (dotted line in the bottom panel of Fig. 2c) and the computed theoretical volumetric outflow rate (dashed line in the bottom panel of Fig. 2c, obtained by subtracting the measured outflow towards all side branches from the measured inflow) was redistributed over all in- and outlets (resulting in the solid lines in Fig. 2c). This redistribution was according to a weighing scheme based on the diameter of the in- and outlets: it was assumed that the largest branch (usually the proximal aorta) was subject to

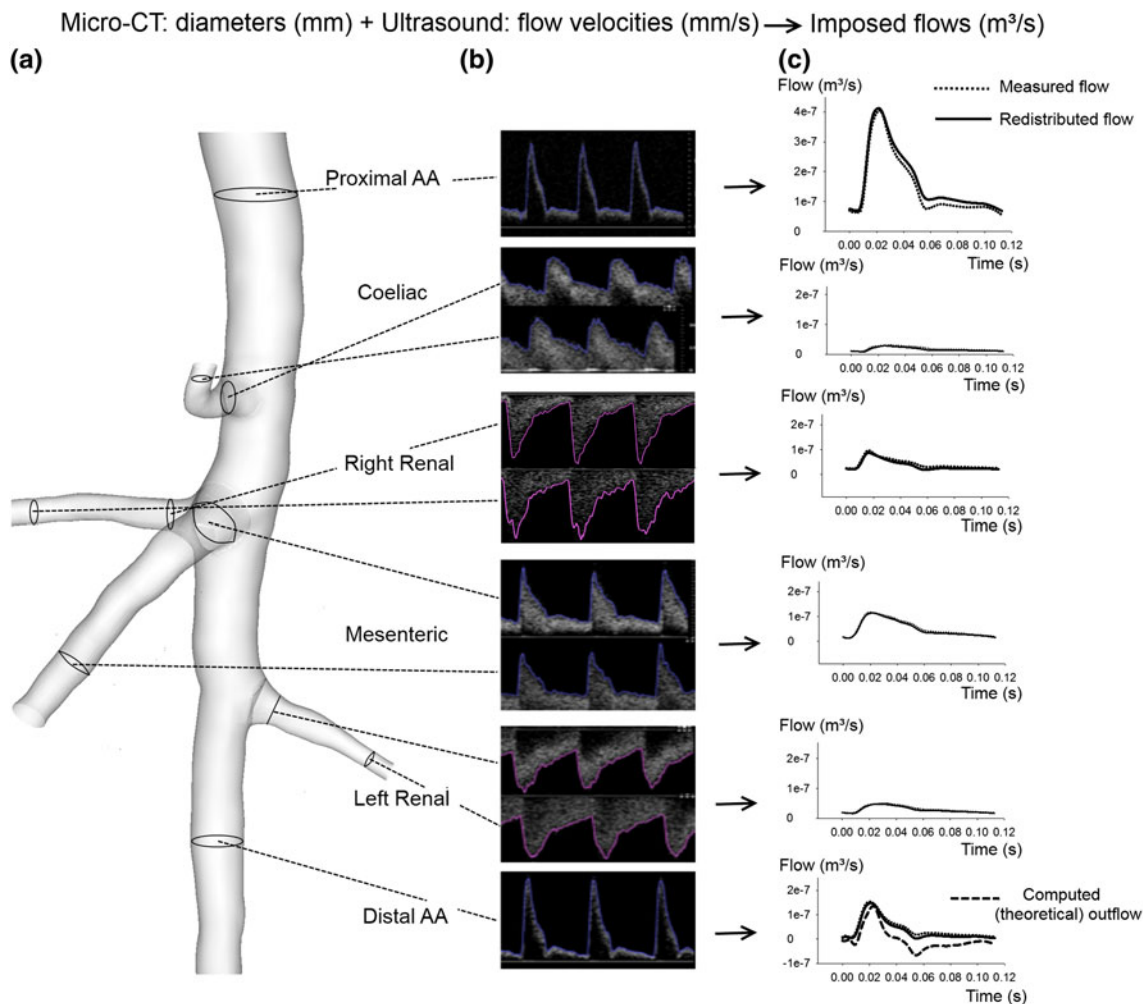


FIGURE 2. Methodology to obtain realistic CFD boundary conditions from the measured flow velocity waveforms, shown for mouse AA6. At each outlet micro-CT diameters (a) are combined with measured US flow velocities (b) to obtain representative flow profiles based on measurements (c, dotted lines). The computed (theoretical) outflow (c, bottom panel, dashed line) is determined subtracting the flow rate to all side branches from the flow rate at the inlet. The error between measured and computed (theoretical) flow rates is then calculated and redistributed over all outlets, and the resulting flow profiles (c, solid lines) are imposed as boundary conditions.

the largest measurement error. The final volumetric flow rate curves were then divided by the cross-sectional area at the respective in- or outlets of the model, to finally obtain flow velocities that can be imposed as boundary conditions in the CFD model. Figure 2 displays how ultrasound measurements were processed for an example case.

Analysis of Measured Flows

All measured ultrasound data were processed as described above and mouse-specific redistributed volumetric flow rates going to each branch are presented in Table 1. Differences between different branches in blood supply and aortic diameter were analyzed using a paired student's test in which a p value smaller than 0.05 was considered significant.

CFD Simulations

All numerical simulations of the flow field were performed with Fluent 6.2 (Ansys, Canonsburg, PA), a commercially available CFD software package. Blood density was taken to be 1060 kg/m^3 and at the high shear rates appropriate for the murine arterial system the dynamic blood viscosity was assumed to remain at a constant asymptotic value of 3.5 mPas .¹⁴ As inflow boundary condition, a parabolic flow velocity profile derived from the volumetric flow waveform was imposed in the proximal abdominal aorta (see above). The time-dependent outflow velocity curves as derived above (Fig. 2) were imposed as parabolic profiles at the outlets of the mesenteric, celiac and left and right renal arteries. To avoid numerical instabilities via imposing flow boundary conditions at all in- and outlets, the distal abdominal aorta was modeled as a traction-free outlet. For each simulation, three cardiac cycles were simulated and all results were obtained from the third cycle, when cycle-to-cycle variability had ceased. The hexahedral mesh consisted of about 500,000 cells, and a mesh-sensitivity analysis was performed in one typical case, increasing the number of cells up to 900,000 to ascertain that a further increase of the number of cells did not influence the results.

Post-processing

Derived CFD data consisted of time-varying 3-dimensional vector fields of the flow velocity in the abdominal aorta and side branches, and these data were further processed using Tecplot (Tecplot Inc., Bellevue, WA). Time-averaged wall shear stress (TAWSS), oscillatory shear index (OSI), and relative residence time (RRT) were calculated, which have

previously been suggested as potential measures of disturbed aortic flow.²⁴

$$\text{TAWSS} = \frac{1}{T} \int_0^T \bar{\tau} \cdot dt$$

$$\text{OSI} = \frac{1}{2} \left(1 - \frac{\left| \frac{1}{T} \int_0^T \bar{\tau} \cdot dt \right|}{\frac{1}{T} \int_0^T |\bar{\tau}| \cdot dt} \right)$$

$$\text{RRT} = \frac{1 - 2 \cdot \text{OSI}}{|\bar{\tau}|}$$

$\bar{\tau}$: Instantaneous wall shear stress vector

T : Period of the cardiac cycle

In order to quantify the correlation between these CFD-based parameters and the location of the aneurysm, the latter needs to be represented by a quantifiable parameter. However, although both baseline and end-stage geometries were obtained in the same animal they did not match one-on-one due to the different position of the animal on the bed. Also, the aorta expanded both in length and in diameter since there was a 5 weeks time period between both scans. To account for these differences, the Vascular Modeling ToolKit (VMTK³) was used to subdivide the end-stage geometry into five separate parts, using natural landmarks such as bifurcations. Each part was then manually co-registered with the corresponding baseline geometry and a distance map was generated to calculate the closest node-to-surface distance from the baseline geometry to that part of the end-stage geometry. These five distance maps were merged to obtain one single distance map which allowed to pinpoint the exact location of the (at that stage yet to be developed) aneurysm on the baseline geometry.

VMTK was used afterwards to divide the aortic surface into patches.⁴ The aorta was subdivided into longitudinal zones with a nominal length of 1 mm, and each longitudinal zone was again subdivided into six circumferential patches. This resulted in a batch of 120–150 patches per aorta, and these were used to calculate the average TAWSS, OSI, RRT, and distance over each patch (see Fig. 3). These patched values were then used afterwards to generate scatter plots (Fig. 6), to enable a quantitative analysis of the results. Patches were divided into three different groups to visualize their longitudinal position along the abdominal aorta. A first group included all patches in the proximal abdominal aorta, while a second group included three layers (18 patches) proximal to the celiac artery as well as all patches between celiac and left renal arteries. A third group included all patches distal from the left

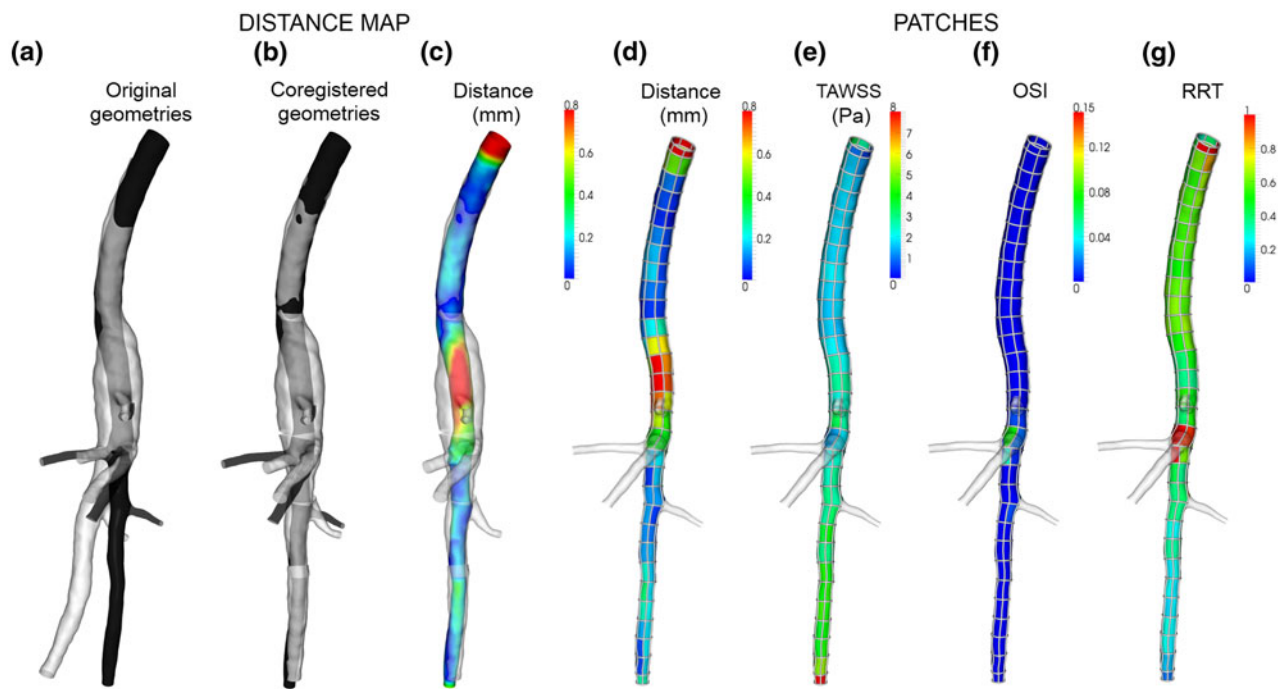


FIGURE 3. Methodology for generation of distance map and patches in mouse AA2. (a) Baseline (black) and end-stage (white) geometries in their original configuration. (b) The end-stage geometry is divided into five parts and each part is co-registered manually to the corresponding baseline geometry. (c) A displacement map is generated indicating the distance from baseline to (co-registered) end-stage in each node. (d) The surface is divided into patches to enable quantification of the results. Each patch is colored with the average distance value of its nodes. (e–g) The patched surface is used to generate patch values of all CFD-based parameters.

renal artery. Dividing the surface in such a structured way thus allowed us to focus on the region of our interest: the aneurismal area of the abdominal aorta.

RESULTS

Of the 10 mice included in the study (indicated as AA*), eight animals survived the complete procedure. One animal (AA3) died 7 days after pump implantation and was therefore further excluded from the study. This animal was found to have severe intra-abdominal bleedings, in accordance with Saraff *et al.*³² who found that on average 10% of the animals die from aortic dissection in the first week. To facilitate analysis of the results, any aortic region in which the distance between the geometry at day 31 and the geometry at baseline expanded with more than 0.3 mm was termed ‘AAA region’. One animal (AA6) was euthanized 18 days after pump implantation for ethical reasons, since it was suffering of a necrotic tail. This animal showed a small dilatation of the abdominal aorta on post-mortem inspection, but was not considered a mouse with developed AAA since the dilatation was smaller than 0.3 mm. In four of the eight remaining animals, the abdominal aorta showed local

dilation >0.3 mm, visually confirmed on post-mortem inspection after 31 days. This is in agreement with previous studies, reporting an incidence of around 50% in male ApoE $-/-$ mice.⁹ The post-mortem diagnosis of AAA was confirmed afterwards based on segmented micro-CT images. The circumferential location of the AAA region was not the same in all animals: in three out of four cases the aneurysm was fusiform (AA1, AA2, AA10), in the fourth animal a saccular aneurysm developed on the left side of the aorta (AA4). The longitudinal location of the AAA region was also varying: in some cases it was limited to the region proximal to the celiac artery (AA4, AA10), in others it included the trifurcation region where mesenteric and right renal artery branch off the aorta (AA1, AA2).

The data presented in Table 1 show the average measured diameters and volumetric flow rates per branch at baseline for every mouse, as well as the fraction of the volumetric flow rate going to each side branch. In general, the mesenteric artery is supplied with the largest fraction of the volumetric flow rate (29%), followed by the distal aorta (25%), right renal artery (20%), left renal artery (15%), and celiac artery (10%). Figure 4 shows streamlines in an example case (mouse AA2) at different timepoints in the cardiac

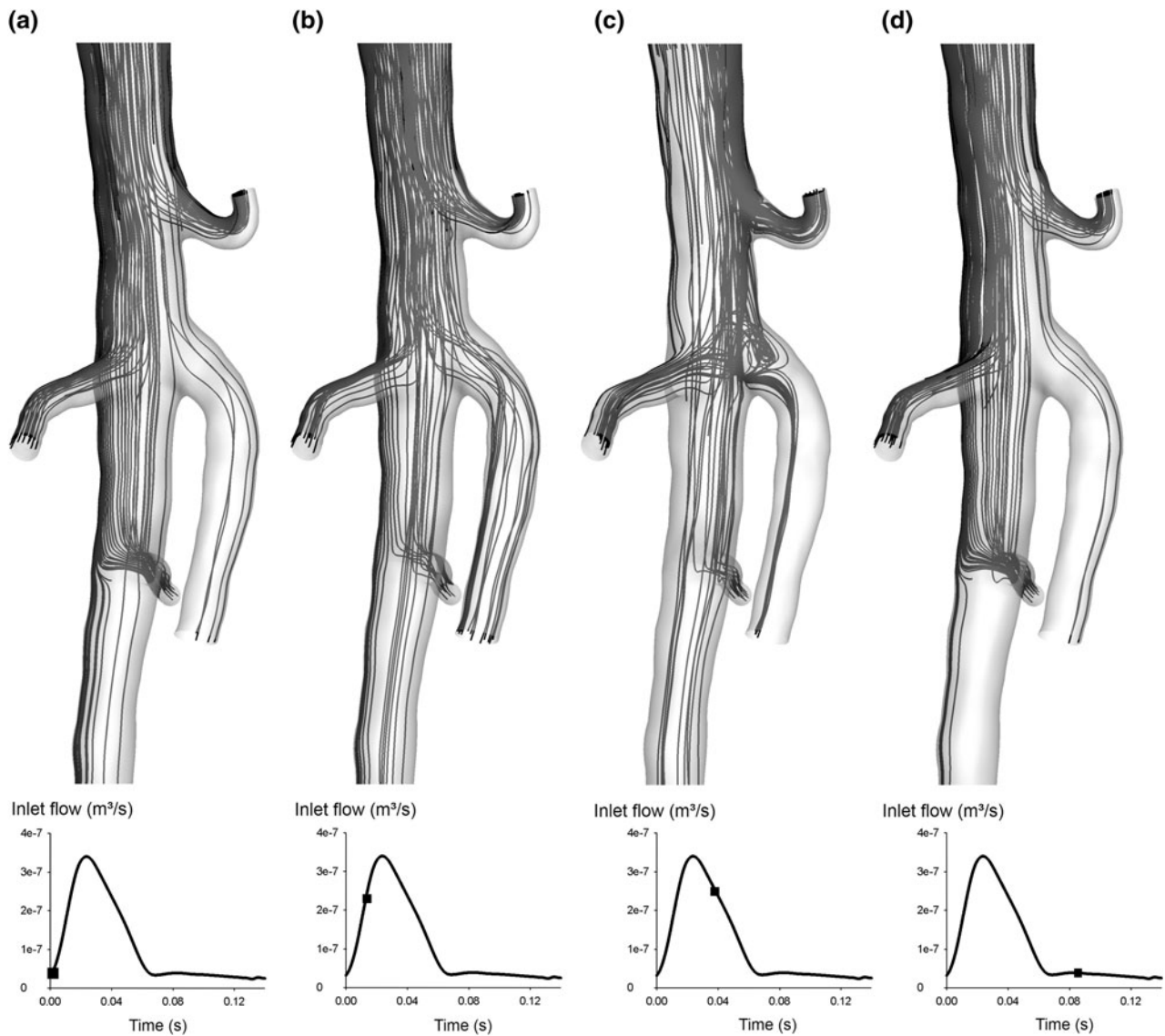


FIGURE 4. Streamlines at different timepoints in the cardiac cycle in mouse AA2.

cycle. These streamlines reveal a very ordered laminar flow throughout the cardiac cycle, only showing some complex laminar flow (recirculation) near the trifurcation immediately after the systolic peak.

Figures 5 and 6, respectively, show a qualitative and a quantitative analysis of the results of CFD simulations in the four cases in which an AAA region could be detected. The qualitative plots for mouse AA2 (Fig. 5a) show a distinct zone of disturbed flow (low TAWSS and high RRT) at the trifurcation, and a similar but less distinct zone just proximal to the celiac artery. The distance map and the end-stage geometry reveal that the aneurysm takes its largest dimension in the aortic region proximal to the celiac artery and extends over the trifurcation region. The patches containing the AAA region (represented by a large

distance to baseline geometry), however, did not experience more disturbed flow compared to other patches along the aorta (Fig. 6a). Also, patches where RRT was highest at baseline (at the trifurcation) are not the ones where AAA region is maximal. The situation in mouse AA4 (Fig. 5b) is similar: there is a small zone of disturbed flow at both the left and right hand side of the celiac artery and at the trifurcation. The AAA region is on the left hand side of the celiac artery, but in a more proximal part of the aorta. Again, the scatter plots for mouse AA4 (Fig. 6b) show that there was no disturbed flow at baseline in the AAA region. Mouse AA10 does not experience seriously disturbed flow, the highest values of RRT occurring at the trifurcation and opposite to the left renal artery (Fig. 5c). The AAA region on the other hand is to be

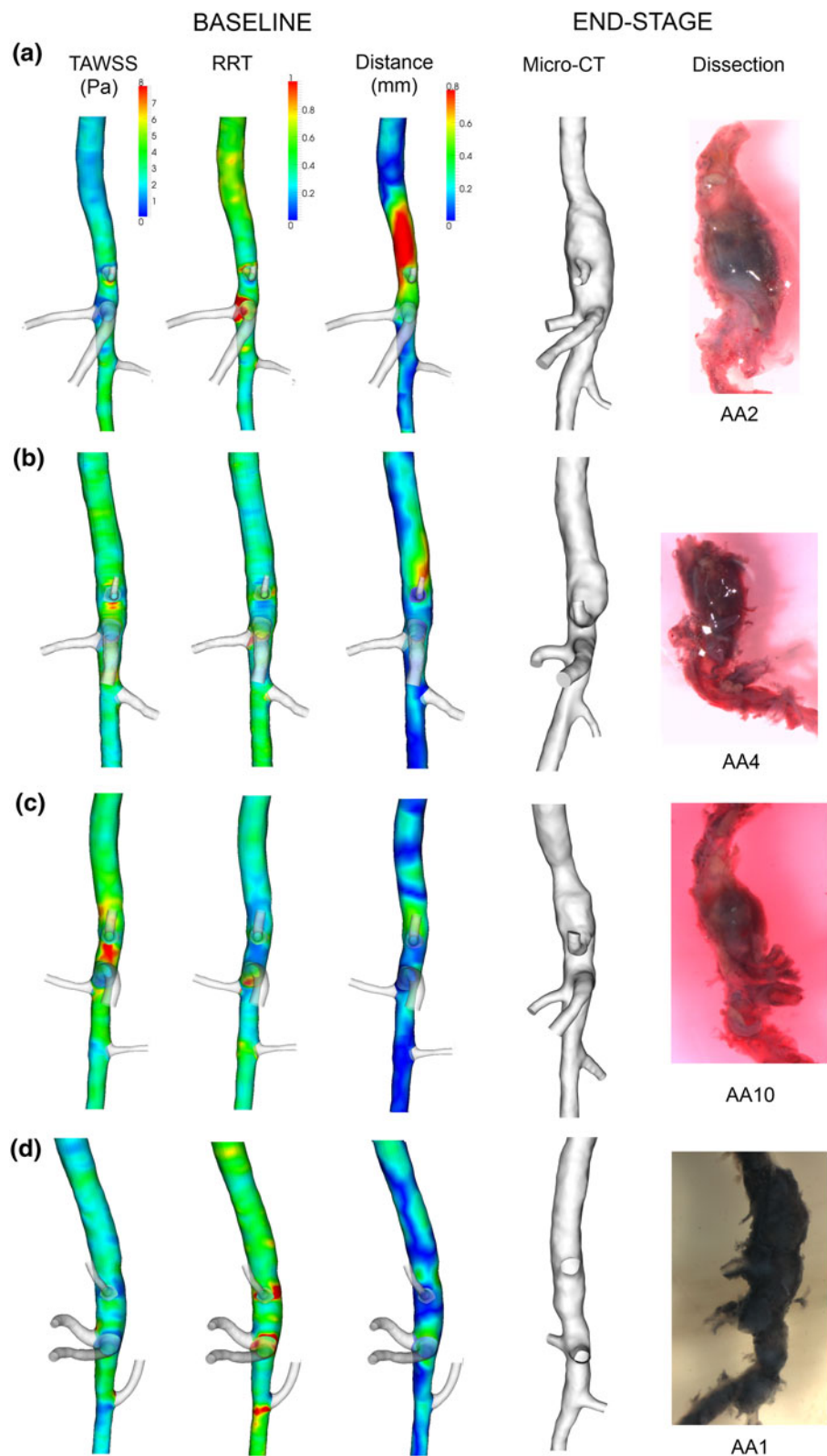


FIGURE 5. Qualitative results. TAWSS, RRT, and distance maps at baseline are shown for all four animals that developed an aneurysm, as well as the corresponding end-stage geometry as obtained from micro-CT images (lumen) and dissection (outer wall, including adventitia). (a) AA2; (b) AA4; (c) AA10; (d) AA1.

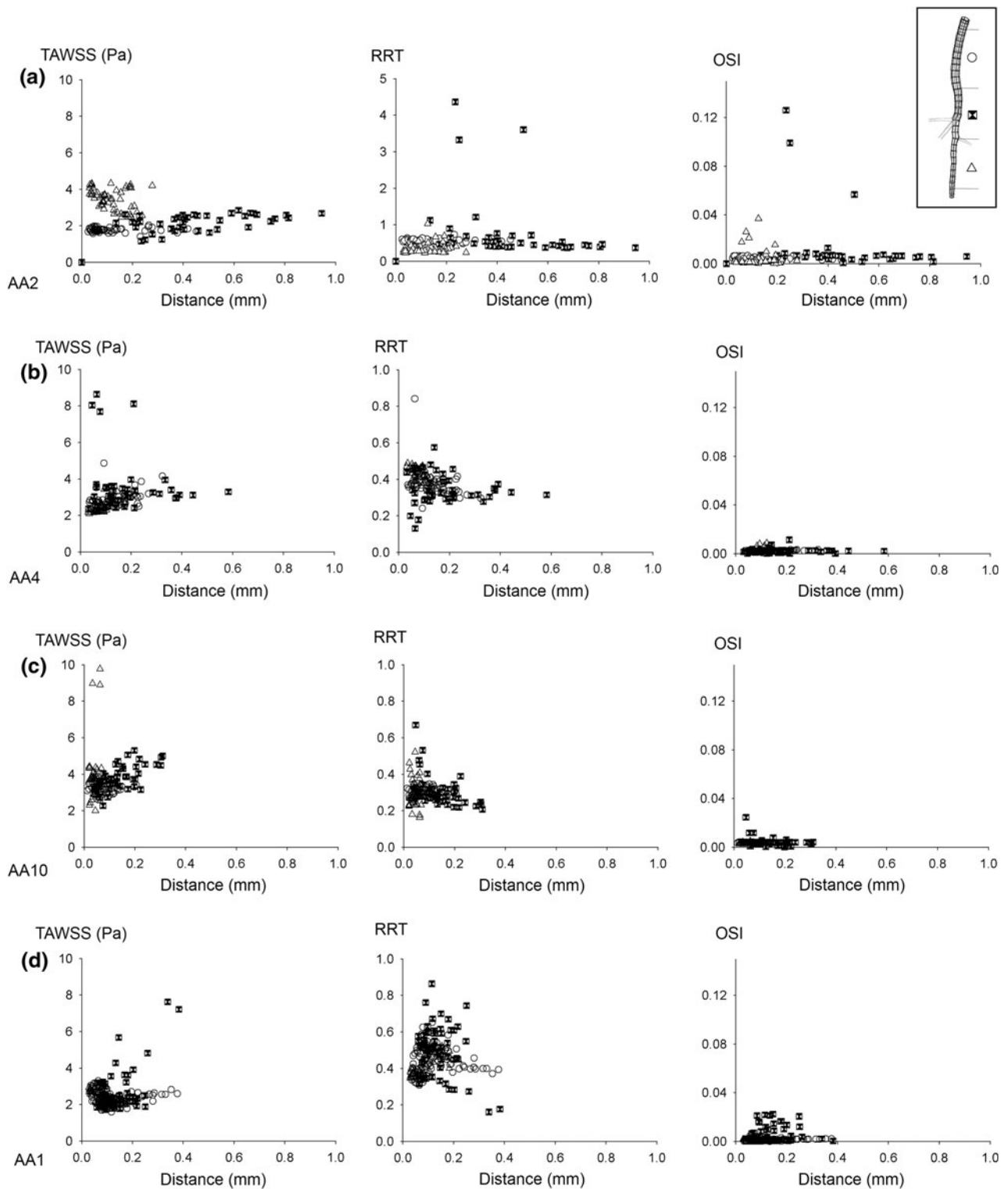


FIGURE 6. Quantitative results. Scatter plots show the relationship between local hemodynamics at baseline and the distance to the corresponding end-stage geometry. Each point represents one patch as obtained via the procedure shown in Fig. 3. Patches were divided into three different groups according to their longitudinal position along the abdominal aorta. Each group was allocated a different symbol. Note that the second figure in (a) was set to a different scale to include outliers. (a) AA2; (b) AA4; (c) AA10; (d) AA1.

found just proximal to the celiac artery, a region in which there was no disturbed flow at all at baseline. This is also reflected in the scatter plots (Fig. 6c), as there is a tendency for TAWSS to be higher and RRT to be lower in the AAA region when compared to other patches. The last mouse in which an AAA region was detected is mouse AA1. Figure 5d shows three regions of disturbed flow at baseline: one distinct zone at the trifurcation and two smaller zones at the level of celiac and left renal arteries. In this case, the aneurysm is located proximal to the celiac artery, extending to the trifurcation region. Again, the scatter plots do not reveal any trivial relation between the studied flow parameters at baseline and the size of the AAA at day 31.

DISCUSSION

We performed mouse-specific CFD simulations of the abdominal aorta in a mouse model of AAA formation to study the relation between intra-aortic hemodynamics and AAA formation. Until recently, the limiting factor to perform such studies was the lack of temporal and spatial resolution in the available imaging modalities. Some studies have performed CFD simulations of the flow field in the mouse aorta basing both geometry and boundary conditions on MRI,²¹ but although in recent work an isotropic voxel resolution of up to $117 \mu\text{m}^3$ has been reached in mice,¹⁸ the resolution is in most cases not sufficient to capture flow in the (smaller) side branches. In literature, most CFD simulations in the mouse aorta base their arterial geometry on a vascular cast, a plastic replica of the arterial system which is subsequently scanned *in vitro* using micro-CT.^{14,22,36,37} Obviously, this technique excludes longitudinal studies, since the mouse needs to be sacrificed. The recent introduction of contrast agents for micro-CT has allowed to circumvent this problem.³⁸ Due to these contrast agents the aorta can be differentiated from surrounding tissues, and it is no longer necessary to sacrifice the animal to obtain a 3D geometry of its arterial system. Apart from the geometry, boundary conditions are indispensable to prescribe the flow rate at the in- and outlets of the model. In literature, most CFD studies working with murine data impose a fixed volumetric flow rate (throughout the cardiac cycle) to all side branches. These fixed volumetric flow rates are in some studies (partially) based on mouse-specific flow velocity measurements using ultrasound or MRI^{14,22} and in other studies on literature data obtained in different mice.^{36,37} In this paper, a novel methodology was used to obtain time-dependent volumetric flow rate profiles *in vivo* in all necessary branches, combining flow velocity measurements (based on high-frequency ultrasound) and diameter measurements (based on

contrast-enhanced micro-CT). Over the length of an arterial segment (not including any side branches), flow velocity can change significantly due to tapering, whereas volumetric flow rate remains constant. Moreover, although ultrasound is a reliable technique it has some drawbacks: it is operator-dependent and it is not always possible to obtain good measurements at all locations throughout the arterial tree. Therefore, an important advantage of the inclusion of diameter data from micro-CT is that it allows to measure ultrasound flow velocities at the location where quality of the pulsed Doppler signal is optimal.

Our methodology corrected for a possible mismatch between different measurements, and resulted in a set of time-dependent mouse-specific volumetric flow rate profiles, compatible with each other throughout the cardiac cycle. These data, listed in Table 1 (and used for the CFD simulations), provide new insight into how the flow is distributed to the different branches in the mouse abdominal aorta, and can therefore be used as reference values for future research. The presented data were obtained after redistributing the error in the mass balance at the outlet over all branches. The redistribution had some influence on the final flow values (mean differences: PAA 0.16 mL/s (11%); CA 0.02 mL/s (15%); MA 0.04 mL/s (13%); RRA 0.03 mL/s (11%); LRA 0.02 mL/s (11%); DAA 0.06 mL/s (18%)). However, without this redistribution the theoretical volumetric outflow rate showed—in some cases—phases of negative flow which were not present in the measured outflow signal of these animals. There are several reasons as to why an error in the mass balance is inevitable: (i) not all branches between the inlet and the outlet of the model have been taken into account. Several smaller branches, such as the middle suprarenal arteries, inferior phrenic artery, gonadal artery, and spinal branches were neglected since they were too small to be segmented with sufficient accuracy from the micro-CT images. Also, it would have been difficult to measure flow velocity to all these side branches within the reasonable timeframe of 1 h; (ii) the actual aorta has a buffer capacity that allows it to distend over time, therefore the flow waveform arrives at a later time point in the cardiac cycle further downstream the aorta. Our CFD simulation is based on a rigid model, which not only implies that the computed wall shear stresses are expected to be higher than what would be the case in a distensible model, but also that at all moments in time the sum of flows at outlets should equal the flow at the inlet. This is incompatible with the (minute) time shift that exists between the measurements. Therefore, measurements of flow in the proximal and distal aorta were not performed at the physical location of the in- and outlets of the model, but close to the location of the side

branches. Since there were no side branches between the measurement location and the model inlet, the mean value of the volumetric flow rate is the same, but the time shift between different measurements is much smaller. This allowed us to subtract outlet flows from the inlet flow without losing the characteristic time-dependent waveform of the flow profiles.

Taking a closer look at the average flow ratios going to each branch, there is a strong trend ($p = 0.07$) towards a difference in blood supply to the left and right renal arteries. The difference between both renal arteries is also reflected in their size, as the left renal diameter (mean value: 0.43 mm) is significantly smaller than the right renal artery (mean value: 0.54 mm; $p < 0.05$). This difference has not been reported previously and is, to the best of our knowledge, not present in humans. It is interesting to note that, unlike in humans, the right renal artery (and kidney) is located superior to its left counterpart. Thus, reduced flow to the left renal artery may be a simple matter of less flow in the aorta at that distal location. Further data confirm that flow is not only determined by the cross-sectional area of a branch, as the left renal shows a tendency to take on average 50% more flow than the celiac artery ($p = 0.06$), while they have exactly the same average diameter (0.43 mm). Also, flow to the mesenteric artery is not significantly different from flow to the distal abdominal aorta ($p = 0.55$), even if its diameter (mean value: 0.65 mm) is significantly lower than that of the distal aorta (mean value: 0.73 mm) ($p < 0.05$). The presented flow data also illustrate the importance of mouse-specific boundary conditions: simply applying a constant outflow rate based on Murray's law to each branch³⁷ would not hold true in this setting. Noteworthy, a relatively large spread is observed between different animals, especially in the right renal and mesenteric arteries. It should be mentioned that the animals did not fast prior to the scans and had *ad libitum* access to water, which may account for some of the variability in the data. A large fraction of the variation is caused by outliers, but the relative distribution of all flow rates is consistent within each animal. It seems that some animals in general experience much higher flow (in all branches) than others (e.g., AA8).

The *in vivo* obtained flow profiles and geometries were combined to set up a mouse-specific CFD simulation at baseline. Previously, it has been shown that low and oscillatory shear can be linked to atherosclerosis, both in humans^{23,26} and mouse models.⁸ No such data exist for aneurysm formation except for the study of Boussel *et al.*,⁷ who have shown in a quantitative way that a human cerebral aneurysm grows most in the region of lowest time-averaged wall shear stress (TAWSS). However, in this study the aneurysm was

already present at the start of the study so its results are only relevant for aneurysm growth, not for its initial phase. In other studies an existing (cerebral) aneurysm was digitally removed in order to obtain an artificial baseline geometry,^{27,28,34} that served as a basis for a CFD simulation to calculate several hemodynamic parameters that could then be linked to the location of the (removed) aneurysm. The eccentric shape of the cerebral aneurysm makes this operation more feasible than, e.g., for an abdominal aneurysm, but the fundamental problem remains: one must always assume the shape (and boundary conditions) of the original geometry. In our study we could avoid this problem since we ascertained to the actual baseline data.

Streamlines reveal a laminar, very structured flow throughout the cardiac cycle except for systolic deceleration, when a complex laminar flow with recirculating streamlines can be observed near the trifurcation. This laminar flow can be explained when taking into account the Reynolds number (Re), a key dimensionless parameter in fluid dynamics expressing the ratio of inertial and viscous forces. It allows us to assess whether flow is laminar ($Re < 2000$), turbulent ($Re > 2500$) or in a transition phase ($2000 \leq Re \leq 2500$). In our simulations the average Re is 40, whereas a typical value in a human abdominal aorta would be around 200.¹⁶ We did not find a direct, trivial correlation between areas of disturbed flow (low TAWSS, high OSI, high RRT) and location of aneurysm formation in the animals developing AAA (AA1, AA2, AA4, and AA10). However, we did observe some recurring patterns when analyzing the results of CFD simulations: the most distinct area of disturbed flow often occurs at the trifurcation, where mesenteric and right renal artery branch off the aorta (AA2, AA4, and AA1). This can also be observed in Fig. 4, where a small recirculation zone is present in the trifurcation area immediately following the systolic peak. Furthermore, smaller areas of disturbed flow occur in the region of celiac (AA2, AA4, and AA1) and, to a lesser extent, left renal artery (AA10, AA1). Note, however, that the absence of correlation between the area of disturbed flow and the location at which the aorta is dilated most, does not necessarily mean that hemodynamics do not influence AAA formation. In three out of four mice (AA2, AA4, AA10) the zone where the AAA region is maximal and the zone of disturbed flow are located at the same side of the aorta, and the AAA region is located proximal to the zone of disturbed flow. From a hemodynamic point of view, one might speculate that AAA formation is initiated at a location that suffers from disturbed flow at baseline (the trifurcation in AA2 and AA1, the celiac artery in AA4). Once a (small) dilatation is established, areas of

disturbed flow would arise in the proximal part of this dilatation, as is the case in an actual aneurysm.¹⁵ Therefore, if AAA formation does depend on the local hemodynamics, one would expect the AAA to originate proximally to the area at which disturbed flow occurs at baseline. Even though the AAA area is not systematically overlapping with the area of disturbed flow at baseline, this hypothesis is (partly) confirmed by the current results, although one would need additional intermediate data to confirm it.

The short-time effect of pump implantation on abdominal hemodynamics is unclear. Although there are no data that would support this theory, we cannot exclude the possibility that pump implantation itself causes a sudden change in hemodynamics (e.g., due to geometric deformation of the aorta). It might thus be beneficial to obtain a set of extra ‘baseline’ data just after pump implantation. Furthermore, it is an open question why the incidence of AAA after pump implantation in male ApoE $-/-$ mice is not higher than 50%. In this paper we were mainly interested in the relationship between hemodynamics and AAA formation in those animals that do develop an AAA and as such we considered it beyond the scope of this work to hypothesize on this incidence rate.

We decided to limit our geometrical model to the abdominal aorta and its most important side branches. Similar to our reasoning about the small abdominal side branches, reduction of scanning time was the main argument not to include the aortic arch (and the three great vessels branching off it) into our model. This decision was further supported by the fact that the aortic arch is not included in most CFD models of the human abdominal aorta found in literature.^{6,25,41} We modeled the velocity flow profile entering the abdominal aorta as a non-skewed, fully developed parabolic profile. In reality, however, blood enters the descending thoracic aorta as a skewed profile, due to the particular bending of the arch.³³ Including this rotational part of the flow into the inlet boundary condition of our model might therefore influence the distribution over the aorta of several of the calculated hemodynamic parameters.³⁵ Furthermore, the ApoE $-/-$ mouse model infused with Angiotensin II has recently been reported to develop thoracic aortic aneurysms in some cases as well.¹² This is an important finding, since the presence of an aneurysm in the proximal part of the aorta might influence the flow profile entering the abdominal aorta.

We calculated a distance map to represent the growth from baseline to end-stage geometry in the four animals that developed an AAA. The main goal of the distance map was to identify the AAA zone on the baseline geometry, thus enabling a comparison with CFD data in a quantitative way. A simple automatic

rigid co-registration of the baseline and end-stage geometries (Fig. 3a) did not suffice to generate a reliable distance map on the baseline surface. Subdividing the end-stage geometry into five subparts allowed us to overcome the effect of the different bending of the aorta in both geometries (Fig. 3b). However, this co-registration is still fairly rigid and therefore in some locations the generated distance map will still be sub-optimal (e.g., the distal abdominal aorta in Fig. 3b). However, we believe that the artificial distance caused by this suboptimal positioning is negligible when compared to the distance at the location of the aneurysm. It is in any case impossible to match both geometries one-on-one since—due to the 5 weeks period between both scans—the aorta has not only expanded in diameter but also in length, causing an increase in the distance between different landmarks (e.g., celiac bifurcation, mesenteric, and right renal trifurcation) as well. We have chosen to optimize the position of the part containing the aneurysm itself, which in some cases implies a slight longitudinal mismatch in proximal and distal parts of the aorta.

The size of the patches was determined in such a way that contingent local spurious flow features were averaged out, but sufficient detail was maintained to distinguish different zones from each other based on their hemodynamic conditions. Patches on the different side branches were not taken into account since we are only interested in locating the region of the aortic wall that is most prone to AAA development. Since the scans of both geometries in general did not contain the exact same aortic length, superfluous patches at in and/or outlets were dismissed in the quantitative analysis, as were patches at in- and outlets that contained artificially high WSS values due to the inlet conditions.

Throughout this work, we have used the term ‘AAA region’ for all aortic regions in which the difference in distance between the end-stage and the baseline lumen was greater than 0.3 mm. This is a somewhat artificial definition not based on clinical practice (where an aneurysm is defined as a dilatation of at least 1.5 times the local diameter). However, we believe that it is justified to use this term even for small dilatations, since we do not use it as the basis for a clinical decision but are mainly interested in AAA initiation itself. The presence of AAA was initially based on a macroscopic evaluation of the aorta just after autopsy. All animals were dissected on the same day the last micro-CT scan was performed, and in general there is a good agreement in the macroscopic shape of the AAA between images obtained from autopsy and end-stage micro-CT (Fig. 5). One can observe that the AAA region often looks smaller in the micro-CT images (e.g., AA1 in Fig. 5d). This is mainly due to the fact that the micro-CT geometry is based on the (segmented) lumen.

However, it is known that medial and adventitial remodeling occur (see Saraff *et al.*³²) which may in some cases cause significant differences between the circumferential shape of interior and exterior AAA wall. Consequently, the calculated distance map in these particular cases (e.g., AA1) may not correspond entirely to the actual aneurysmatic region.

CONCLUSION

We set up an experimental-computational framework combining flow velocity measurements (based on high-frequency ultrasound) and diameter measurements (based on contrast-enhanced micro-CT) to set up mouse-specific CFD simulations of the hemodynamic situation in the mouse abdominal aorta, only based on *in vivo* data. We applied the methodology in an established mouse model of AAA to investigate the relation between the presence of disturbed hemodynamics at baseline and the formation of abdominal aortic aneurysm (AAA). We observed significant inter-individual variability in hemodynamic characteristics of the abdominal aorta, emphasizing the importance of mouse-specific analysis. The most distinct area of disturbed flow was in most cases either at the trifurcation (where mesenteric and right renal artery branch off) or at the bifurcation where the celiac artery branches off the aorta. Qualitative results showed that for the animals which developed AAA, AAA dimension is maximal in areas that are situated proximal to those areas that experience most disturbed flow in three out of four mice. Although further detailed analysis did not reveal any obvious relationship between areas that experience most disturbed flow and the end-stage AAA dimensions (and therefore excludes a conclusive message), the results of this study do not exclude that hemodynamics do play a role in AAA formation. Due to its mouse-specific and *in vivo* nature, the presented methodology can be used in future research to link detailed and animal-specific (baseline) hemodynamics to (end-stage) arterial disease in longitudinal studies in mice.

ACKNOWLEDGMENTS

This research was funded by the Special Research Fund of the Ghent University (BOF10/GOA/005) and the Hercules Foundation (project AUGE/09/012). Bram Trachet is recipient of a research grant of the Flemish government agency for Innovation by Science and Technology (IWT). The authors wish to

acknowledge the assistance of Philippe Joye and Scharon Bruneel from the Ghent University small animal imaging lab (INFINITY).

CONFLICTS OF INTEREST

There are no conflicts of interests to be declared.

REFERENCES

- ¹Alexander, J. J. The pathobiology of aortic aneurysms. *J. Surg. Res.* 117:163–175, 2004.
- ²Amirbekian, S., R. C. Long, M. A. Consolini, J. Suo, N. J. Willett, S. W. Fielden, D. P. Giddens, W. R. Taylor, and J. N. Oshinski. In vivo assessment of blood flow patterns in abdominal aorta of mice with MRI: implications for AAA localization. *Am. J. Physiol. Heart Circ. Physiol.* 297: H1290–H1295, 2009.
- ³Antiga, L., and D. A. Steinman. <http://www.vmtk.org>.
- ⁴Antiga, L., and D. A. Steinman. Robust and objective decomposition and mapping of bifurcating vessels. *IEEE Trans. Med. Imaging* 23:704–713, 2004.
- ⁵Barisione, C., D. L. Rateri, J. J. Moorlegghen, D. A. Howatt, and A. Daugherty. Angiotensin II infusion promotes rapid dilation of the abdominal aorta detected by noninvasive high frequency ultrasound. *Arterioscler. Thromb. Vasc. Biol.* 26:E73, 2006.
- ⁶Biasetti, J., T. C. Gasser, M. Auer, U. Hedin, and F. Labruto. Hemodynamics of the normal aorta compared to fusiform and saccular abdominal aortic aneurysms with emphasis on a potential thrombus formation mechanism. *Ann. Biomed. Eng.* 38:380–390, 2010.
- ⁷Boussel, L., V. Rayz, C. McCulloch, A. Martin, G. Acevedo-Bolton, M. Lawton, R. Higashida, W. S. Smith, W. L. Young, and D. Saloner. Aneurysm growth occurs at region of low wall shear stress: patient-specific correlation of hemodynamics and growth in a longitudinal study. *Stroke* 39:2997–3002, 2008.
- ⁸Cheng, C., D. Tempel, R. van Haperen, A. van der Baan, F. Grosveld, M. J. A. P. Daemen, R. Krams, and R. de Crom. Atherosclerotic lesion size and vulnerability are determined by patterns of fluid shear stress. *Circulation* 113:2744–2753, 2006.
- ⁹Daugherty, A., and L. Cassis. Angiotensin II and abdominal aortic aneurysms. *Curr. Hypertens. Rep.* 6:442–446, 2004.
- ¹⁰Daugherty, A., and L. A. Cassis. Mouse models of abdominal aortic aneurysms. *Arterioscler. Thromb. Vasc. Biol.* 24:429–434, 2004.
- ¹¹Daugherty, A., M. W. Manning, and L. A. Cassis. Angiotensin II promotes atherosclerotic lesions and aneurysms in apolipoprotein E-deficient mice. *J. Clin. Invest.* 105:1605–1612, 2000.
- ¹²Daugherty, A., D. L. Rateri, I. F. Charo, A. P. Owens, D. A. Howatt, and L. A. Cassis. Angiotensin II infusion promotes ascending aortic aneurysms: attenuation by CCR2 deficiency in apoE $-/-$ mice. *Clin. Sci.* 118:681–689, 2010.
- ¹³De Santis, G., P. Mortier, M. De Beule, P. Segers, P. Verdonck, and B. Verheghe. Patient-specific computational fluid dynamics: structured mesh generation from

- coronary angiography. *Med. Biol. Eng. Comput.* 48:371–380, 2010.
- ¹⁴Feintuch, A., P. Ruengsakulrach, A. Lin, J. Zhang, Y. Q. Zhou, J. Bishop, L. Davidson, D. Courtman, F. S. Foster, D. A. Steinman, R. M. Henkelman, and C. R. Ethier. Hemodynamics in the mouse aortic arch as assessed by MRI, ultrasound, and numerical modeling. *Am. J. Physiol. Heart Circ. Physiol.* 292:H884–H892, 2007.
- ¹⁵Finol, E. A., and C. H. Amon. Blood flow in abdominal aortic aneurysms: pulsatile flow hemodynamics. *J. Biomech. Eng.* 123:474–484, 2001.
- ¹⁶Finol, E. A., K. Keyhani, and C. H. Amon. The effect of asymmetry in abdominal aortic aneurysms under physiologically realistic pulsatile flow conditions. *J. Biomech. Eng.* 125:207–217, 2003.
- ¹⁷Goergen, C. J., J. Azuma, K. N. Barr, L. Magdefessel, D. Y. Kallop, A. Gogineni, A. Grewall, R. M. Weimer, A. J. Connolly, R. L. Dalman, C. A. Taylor, P. S. Tsao, and J. M. Greve. Influences of aortic motion and curvature on vessel expansion in murine experimental aneurysms. *Arterioscler. Thromb. Vasc. Biol.* 31:270–279, 2011.
- ¹⁸Goergen, C. J., K. N. Barr, D. T. Huynh, J. R. Eastham-Anderson, G. Choi, M. Hedehus, R. L. Dalman, A. J. Connolly, C. A. Taylor, P. S. Tsao, and J. M. Greve. In vivo quantification of murine aortic cyclic strain, motion, and curvature: implications for abdominal aortic aneurysm growth. *J. Magn. Reson. Imaging* 32:847–858, 2010.
- ¹⁹Golledge, J., J. Muller, A. Daugherty, and P. Norman. Abdominal aortic aneurysm—pathogenesis and implications for management. *Arterioscler. Thromb. Vasc. Biol.* 26:2605–2613, 2006.
- ²⁰Gordon, I. L., C. A. Kohl, M. Arefi, R. A. Complin, and M. Vulpe. Spinal cord injury increases the risk of abdominal aortic aneurysm. *Am. Surg.* 62:249–252, 1996.
- ²¹Greve, J. M., A. S. Les, B. T. Tang, M. T. D. Blomme, N. M. Wilson, R. L. Dalman, N. J. Pelc, and C. A. Taylor. Allometric scaling of wall shear stress from mice to humans: quantification using cine phase-contrast MRI and computational fluid dynamics. *Am. J. Physiol. Heart Circ. Physiol.* 291:H1700–H1708, 2006.
- ²²Huo, Y. L., X. M. Guo, and G. S. Kassab. The flow field along the entire length of mouse aorta and primary branches. *Ann. Biomed. Eng.* 36:685–699, 2008.
- ²³Ku, D. N., D. P. Giddens, C. K. Zarins, and S. Glagov. Pulsatile flow and atherosclerosis in the human carotid bifurcation—positive correlation between plaque location and low and oscillating shear—stress. *Arteriosclerosis* 5:293–302, 1985.
- ²⁴Lee, S. W., L. Antiga, and D. A. Steinman. Correlations among indicators of disturbed flow at the normal carotid bifurcation. *J. Biomech. Eng. Trans. ASME.* 131, 2009.
- ²⁵Les, A. S., S. C. Shadden, C. A. Figueroa, J. M. Park, M. M. Tedesco, R. J. Herfkens, R. L. Dalman, and C. A. Taylor. Quantification of hemodynamics in abdominal aortic aneurysms during rest and exercise using magnetic resonance imaging and computational fluid dynamics. *Ann. Biomed. Eng.* 38:1288–1313, 2010.
- ²⁶Malek, A. M., S. L. Alper, and S. Izumo. Hemodynamic shear stress and its role in atherosclerosis. *JAMA* 282:2035–2042, 1999.
- ²⁷Mantha, A., C. Karmonik, G. Benndorf, C. Strother, and R. Metcalfe. Hemodynamics in a cerebral artery before and after the formation of an aneurysm. *Am. J. Neuroradiol.* 27:1113–1118, 2006.
- ²⁸Meng, H., Z. Wang, Y. Hoi, L. Gao, E. Metaxa, D. D. Swartz, and J. Kolega. Complex hemodynamics at the apex of an arterial bifurcation induces vascular remodeling resembling cerebral aneurysm initiation. *Stroke* 38:1924–1931, 2007.
- ²⁹Moore, J. E., C. P. Xu, S. Glagov, C. K. Zarins, and D. N. Ku. Fluid wall shear stress measurements in a model of the human abdominal aorta—oscillatory behavior and relationship to atherosclerosis. *Atherosclerosis* 110:225–240, 1994.
- ³⁰Patel, M. I., D. T. A. Hardman, and C. M. Fisher. Current views on the pathogenesis of abdominal aortic aneurysms. *J. Am. Coll. Surg.* 181:371–382, 1995.
- ³¹Sakalihasan, N., R. Limet, and O. D. Defawe. Abdominal aortic aneurysm. *Lancet* 365:1577–1589, 2005.
- ³²Saraff, K., F. Babamusta, L. A. Cassis, and A. Daugherty. Aortic dissection precedes formation of aneurysms and atherosclerosis in angiotensin II-infused, apolipoprotein E-deficient mice. *Arterioscler. Thromb. Vasc. Biol.* 23:1621–1626, 2003.
- ³³Shahcheraghi, N., H. A. Dwyer, A. Y. Cheer, A. I. Barakat, and T. Rutaganira. Unsteady and three-dimensional simulation of blood flow in the human aortic arch. *J. Biomech. Eng. Trans. ASME* 124:378–387, 2002.
- ³⁴Shimogonya, Y., T. Ishikawa, Y. Imai, N. Matsuki, and T. Yamaguchi. Can temporal fluctuation in spatial wall shear stress gradient initiate a cerebral aneurysm? A proposed novel hemodynamic index, the gradient oscillatory number (GON). *J. Biomech.* 42:550–554, 2009.
- ³⁵Shipkowitz, T., V. G. J. Rodgers, L. J. Frazin, and K. B. Chandran. Numerical study on the effect of secondary flow in the human aorta on local shear stresses in abdominal aortic branches. *J. Biomech.* 33:717–728, 2000.
- ³⁶Suo, J., D. E. Ferrara, D. Sorescu, R. E. Guldberg, W. R. Taylor, and D. P. Giddens. Hemodynamic shear stresses in mouse aortas—implications for atherogenesis. *Arterioscler. Thromb. Vasc. Biol.* 27:346–351, 2007.
- ³⁷Trachet, B., A. Swillens, D. Van Loo, C. Casteleyn, A. De Paep, B. Loeys, and P. Segers. The influence of aortic dimensions on calculated wall shear stress in the mouse aortic arch. *Comput. Methods Biomech. Biomed. Eng.* 12:491–499, 2009.
- ³⁸Vandeghinste, B., B. Trachet, M. Renard, C. Casteleyn, S. Staelens, B. Loeys, P. Segers, and S. Vandenberghe. Replacing vascular corrosion casting by in vivo micro-CT imaging for building 3D cardiovascular models in mice. *Mol. Imaging Biol.* 13:78–86, 2011.
- ³⁹Verhegge, B. <http://www.pyFormex.org>.
- ⁴⁰Vollmar, J. F., P. Pauschinger, E. Paes, E. Henze, and A. Friesch. Aortic aneurysms as late sequelae of above-knee amputation. *Lancet* 2:834–835, 1989.
- ⁴¹Yeung, J. J., H. J. Kim, T. A. Abbruzzese, I. E. Vignon-Clementel, M. T. Draney-Blomme, K. K. Yeung, I. Perikash, R. J. Herfkens, C. A. Taylor, and R. L. Dalman. Aortoiliac hemodynamic and morphologic adaptation to chronic spinal cord injury. *J. Vasc. Surg.* 44:1254–1265, 2006.